Deciphering non-covalent interactions of 1,3-Benzenedimethanaminium bis(trioxonitrate): Synthesis, empirical and computational study

Sofian Gatfaoui, Noureddine Issaoui, Silvia Antonia Brandan, Mouna Medimagh, Omar Al-Dossary, Thierry Roisnel, Houda Marouani, Aleksandr S. Kazachenko

▶ To cite this version:

Sofian Gatfaoui, Noureddine Issaoui, Silvia Antonia Brandan, Mouna Medimagh, Omar Al-Dossary, et al.. Deciphering non-covalent interactions of 1,3-Benzenedimethanaminium bis(trioxonitrate): Synthesis, empirical and computational study. Journal of Molecular Structure, 2022, 1250, pp.131720. 10.1016/j.molstruc.2021.131720 . hal-03476815

HAL Id: hal-03476815
https://hal.science/hal-03476815v1

Deciphering non-covalent interactions of 1,3-Benzenedimethanaminium bis(trioxonitrate): Synthesis, empirical and computational study

Sofian Gatfaoui[a], Noureddine Issaoui[b]*, Silvia Antonia Brandán[c], Mouna Medimagh[b], Omar Al-Dossary[d], Thierry Roisnel[e] and Houda Marouani[a], Aleksandr S. Kazachenko[f,g]

[a] University of Carthage, Faculty of Sciences of Bizerte, LR13ES08 Laboratory of Materials chemistry, 7021, Bizerte,Tunisia
[b]University of Monastir, Laboratory of Quantum and Statistical Physics LR18ES18, Faculty of Sciences, Monastir 5079, Tunisia
[c]Cátedra de Química General, Instituto de Química Inorgánica, Facultad de Bioquímica. Química y Farmacia, Universidad Nacional de Tucumán, Ayacucho 471, (4000) San Miguel de Tucumán, Tucumán, Argentina
[d]Department of Physics and Astronomy, College of Science, King Saud University, PO Box 2455, Riyadh, 11451 Saudi Arabia
[e]Univ Rennes, CNRS, ISCR (Institut des Sciences Chimiques de Rennes) – UMR 6226, F-35000 Rennes, France
[f]Institute of Chemistry and Chemical Technology SB RAS, Federal Research Center "Krasnoyarsk Science Center SB RAS", Akademgorodok, 50/24, Krasnoyarsk, 660036, Russia
[g]Siberian Federal University, Svobodny av., 79, Krasnoyarsk, 660041, Russia

*Correspondence e-mail: issaoui_noureddine@yahoo.fr

Highlights

- A new organic–inorganic hybrid nitrate was synthesized at room temperature.
- The atomic arrangement shows three-dimensional network.
- Quantum mechanical calculations were performed using the DFT method and topological analyzes.
- IR spectroscopy, thermal and electrical measurement was investigated.
- The biological activity was performed via molecular docking analysis.

Abstract

1,3-Benzenedimethanaminium bis(trioxonitrate), denoted by **BD(NO_3)$_2$** was prepared and its structure determined by X-ray crystallography. This compound solidifies into the triclinic system and the $P2_1/c$ space group with the lattice parameters a = 21.4308 (7) Å, b = 5.7255 (2) Å, c = 20.4476 (5) Å, β = 108.502 (1) °, V = 2379.28 (13) Å^3, Z = 8, R = 0.047 and Rw = 0.129. In the crystal, the ions are allied by a huge number of N-H···O hydrogen bonds, creating layers parallel to (100). These layers are associated by hydrogen bonding type C-H···O, endorsing consequently a 3D arrangement. B3LYP/6-311++G**calculations were carried out to analyze the structure and properties of **BD(NO_3)$_2$**. Intermolecular contacts involved in the selection and packaging of the crystalline structure of **BD(NO_3)$_2$** were investigated using fingerprint traces of the Hirshfeld surface. HOMO and LUMO analyses explain the charge transfers within the molecule. Topological analysis, RDG, molecular electrostatic potential (MEP) have been processed to calculate the intermolecular H-bonds interactions in detail. Thermal fusion and decomposition were investigated using TG, DTA and DSC measurements. Ionic conduction (H^+) has been intentional in the temperature range 323 to 393 K, indicating semiconductor behaviour of the material produced. Complete assignments of bands observed in the FTIR spectrum were reported together with the main force constants. The presence of dimeric species is important to explain why the intense bands predicted for the monomer due to N-H···O-N interactions are not observed in the experimental IR spectrum. The biological activity of **BD(NO_3)$_2$** was accomplished *in silico* to investigate their antibacterial activity.

Keywords: X-ray diffraction, DFT, TG-DTA, Semiconductor, Molecular docking.

1. Introduction

Chemistry and natural science become nowadays branch of our daily surroundings, the two domains being at the intersection of many sectors and many industries, such as pharmacy, agro-food, environment, biotechnology, constituting so many fields in which professionals in chemistry and biology operate. The organic chemistry of the past increases now, to biological molecules, inorganic molecules and macromolecules. The mixture of organic and inorganic materials inside the same compound provides extraordinary prospects both in provisions of physical effects and chemical reactivity, it is like that by associating organic and mineral entities, a new class, hybrids are appear. These hybrid compounds take a significant part in cell metabolism; they are involved in energy transfer owing to their prosperity in intermolecular interactions passing through hydrogen bonds. These materials are well adopted for applications in such varied fields such as biology, optics, photochemistry, photo catalysis and medicine [1,2]. Especially, the involvement of HNO3 acid with organic entities, aim of our work, produce organic nitrates possessing significant properties in biological systems, for example 1-methypiperazine-1,4-diium dinitrate [3] and 1-ethylpiperazine-1,4-diium bis(nitrate) [4]. Also could escort to non-centrosymmetric assemblages efficient in non-linear optics (3-methylbenzylammonium trioxonitrate) [5]. Within this framework, diverse docking researches have been specified in medicine design [4–8], this discloses that 1EPBN [4] might exhibit inhibitory effects in opposition to the proteins of the coronavirus (COVID-19). Also 1-phenylpiperazin-1,4-diium nitrate monohydrate [9] perforates the active site of both enzymes (Kalirin-7 and MOB), consequently we can judge it as powerful inhibitors of Parkinson's disease, Alzheimer's and Schizophrenia disease. Due to their varied properties, a new organic-inorganic material: 1,3-Benzenedimethanaminium bis(trioxonitrate) was reported, whose general chemical formula is as follows $(C_8H_{14}N_2)(NO_3)_2$. The XRD and DFT first principles approaches were used to fully elucidate our structure and to compare their different geometric properties with other nitrate and with other anions having the same organic cation. DFT method is used to reveal the geometrical parameters, frontier orbital gap provides the knowledge of kinetic stability and chemical reactivity, donor-acceptor interactions, reactive site analysis and electronic analysis [10-12]. Hirshfeld surface analysis (HS) was used to count non-covalent interactions (NCI) and confirmed the importance of bonding networks in the crystalline framework. Investigation by IR absorption spectroscopy of the produced compound enabled us to settle on the vibrational features of the latter using group theory and in particular, the listing of the vibration modes of nitrate ion and the allocation of the observed frequencies of different types of vibratory movements in the NO_3^- group. The thermal study of **$BD(NO_3)_2$**, shows that this material undergoes under the temperature effect a total decomposition in a wide temperature range, leading to black carbon residues and handling to nitrogen oxides. Study of the electrical properties shows that the conductivity (σ) of our compound is 10^{-6} $S.cm^{-1}$ order with an activation energy not exceeding 1 eV. An important difference between HOMO and LUMO energy means the electron excitation energy which is essential for calculating the molecular reactivity and stability of the title compound. In addition topological analyzes were planned including AIM (atom in molecule), RDG (reduced density gradient) and MEP (molecular electrostatic potential). In particular, xylylenediamine belongs to a polyvalent class of aromatic compounds having three isomers, including the *m*-xylylenediamine, *p*-xylylenediamine and *o*-xylylenediamine derivatives, contingent the relative positions of the two $-CH_2-NH_2$ groups. Among these *m*-xylylenediamine under the systematic name 1,3-Benzenedimethanamine can be treated as a remedy forerunner because it has antibacterial properties [8,9,13], therefore in this context the molecular docking analysis shows that the **$BD(NO_3)_2$** compound has antibacterial activity and it plays an essential function in the detection of drugs for certain diseases.

2. Experimental details

2.1. Synthesis and crystallization of $BD(NO_3)_2$

The title crystal was synthesized under room temperature conditions. Typically an aqueous solution including 4mmol of HNO_3 in 10mL of water was append to 2mmol of 1,3-Benzenedimethanamine in 10mL of water with continuous stirring. The homogenized mixture undergoes evaporation for a few days, comes to saturation and produces colorless prismatic crystals, steady and of appropriate dimension for diffraction study. The solubility test of our crystal in different solvents shows that it is perfectly soluble in water, ethanol and in dimethylsulfoxide (DMSO). The chemical reaction scheme from which crystals are derived is:

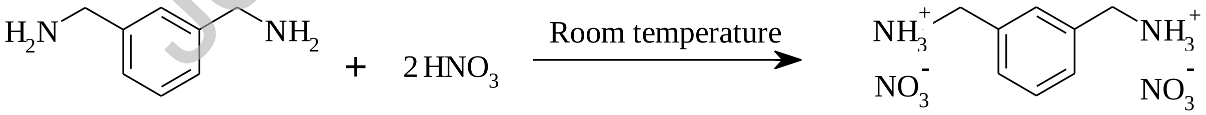

2.2. Materials and measurements

The intensities collections of the X-ray diffracted (XRD) by the single crystal were carried out by a diffractometer Bruker-AXS APEXII type at 150 K, controlled by computer and functioning at the molybdenum wavelength Kα (λ = 0.71073 Å). Absorption corrections were treated by the multi-scan procedure by means of SADABS package [14]. Amid the 19108 reflections measured only 5457 are independent and 4429 had intensity $I > 2\sigma(I)$. The structure was solved using the SIR97 [15] method and refined on F^2 by the full-matrix least squares method using SHELXL-97 [16] to R=0.047, wR=0.129. All non-H atoms were reined anisotropically. An abstract of the crystallographic numbers and the structure refinements are tabulated in Table 1. Structure figures are designed with Diamond program [17].

The IR spectra were brought in a BXII spectrometer by means of a sample dispersed in a spectroscopically pure KBr pastille in the 400–4000 cm^{-1} domain.

The impedance diagrams were put down in the 0.01−13000 kHz frequency range via a Hewlett Packard HP 4192A analyzer with 10 °C steps. The measurements were made over a wide range of temperatures (333–393) K. Using a 7 ton hydraulic press to prepare an **BD(NO_3)$_2$** polycrystalline pellet with a diameter of 13 mm and a thickness of 1.25 mm.

Thermal investigation was accomplished using a multimodule 92 Setaram analyzer working 273 K up to 773 K at an regular heating rate of 10 K.min^{-1} and the simple mass was 18.62 mg for TG /DTA.

2.3. Computational procedures

HS analysis is formed on a 3D graph where the molecules show in contact and another 2D that recaps the complexes data enclosed in a structure and makes it achievable to recognize each type of contact. This examination was skilled by means of the Crystal Explorer program [18].

The geometric optimization for a suitable model of monomer was performed at DFT level by means of the B3LYP functional with the 6-311++G** base set with the Gaussian 09 [19] and the GaussView packages [20]. Here, it is essential to elucidate that the dimeric species was too optimized in gas phase at the similar level of theory as some intense bands observed in the IR spectrum is justified by the presence of this species in the solid phase. AIM and RDG analysis were carried out using Multiwfn software [21] and employed to determine the topological properties. Additionally, the data about the reactive character of **BD(NO_3)$_2$** was accessed by using their MEP and the transition of frontier molecular orbitals.

The molecular docking calculation was investigated using iGEMDOCK software [22]. The bacteria and fungi enzymes crystal structures are provided from the RCSB data bank [23]. In addition, the results of docking were visualized by using discovery studio software [24].

The vibrational study of monomer of BD(NO_3)$_2$ was executed by using the normal internal coordinates (NICs), scaling factors and the SQMFF methodology with the Molvib program [25,26]. The corresponding NICs were similar to those used for other species containing nitrate groups [5,27]. The complete vibrational assignments of monomer were performed taking into account the harmonic force field in gas phase and assignments reported for other nitrate compounds [5,27]. The scaled force constants also were computed from the harmonic force field and later, compared with reported for other nitrate compounds.

3. Results and discussion

3.1. Simultaneous on powder and single crystal XRD and geometry optimization

The powder XRD pattern of the synthesized compound is recorded in Fig.S1. The powder diffractogram shows diffraction lines which appear particularly fine and not widened, which suggests the microscopic character of the synthesized powder. In fact, the deficiency of additional peaks verifies the purity of the entire sample and no trace of crystallized impurity is detected.

Two organic cations and four nitrate anions crystallographically independent exhibit the conformation shown in Fig. 1a. The projection of the **BD(NO$_3$)$_2$** structure along the b axis direction (Fig. 1b) shows the presence of nitrate anions superposed parallel to the (0 0 1) plane in z = 0, 0.25, for N6 / O4 / O5 / O6, N7 / O7 / O8 / O9, N8 / O10 / O11 / O12 and at z = 0.25 and 0.75 for N5 / O1 / O2 / O3, separated by organic groups 1,3-Benzenedimethanaminium by establishment of N−H ... O and C−H ... O hydrogen bonds forming a 3D network. The experimental and theoretical geometric characteristics of the **BD(NO$_3$)$_2$** compound are listed in Table S1. The geometric characteristics of the four independent nitrate anions are slightly different. The distances N5−O1, N6−O5, N7−O7 and N8−O11 are notably the shortest are of the order of 1.23 Å, because O1, O5, O7 and O11 are applied in a single hydrogen bond (Table S2) at the same time that the other nitrogen-oxygen (NO$_3$) distances are much greater, in the neighborhood of 1.26 Å, because their oxygen atoms are involved in two and three H-bonds. These geometrical features have also been detected in further related structures [5,8,28]. Examination of the 1,3-Benzenedimethanaminium cation shows clearly that the bond lengths and angles show no notable deviations from those in other compounds involving the similar organic groups, such as in (C$_8$H$_{14}$N$_2$)$_2$[CdCl$_6$] [8] crystal structure. The aromatic rings are planar by means of an average deviation of 0.0022 Å and form a dihedral angle of 3.85° in the asymmetric unit. In addition, the two ammonium groups of the organic half adopt the *cis* conformation. The inter-planar space between close phenyl rings is in the neighborhood of 4.59 Å, which is a lot longer than 3.80 Å, value necessary for the establishment of π–π stacking [29]. Intermolecular cohesion between anions and cations is ensured by N(C)−H… O hydrogen bond (Table S2). **BD(NO$_3$)$_2$** is very rich in hydrogen bonds; it has fifteen weak bonds subdivided into two types: N−H… O bonds participating in our structure by two linear forms (N1−H1A… O3 and N3−H3C… O3) of donor - acceptor distances are equal respectively 2.954 (2) Å and 2.889 (19) Å, and nine bifurcated forms involving the H1B, H1C, H2B, H2C, H3A, H3B, H4A, H4B and H4C atoms. These bonds give $R_1^2(4)$, $R_4^2(8)$, $R_6^4(14)$, and $\mathrm{R}_4^3(10)$ cycles (Fig. S2), they are considered weak according to the Brown criterion ($d_{N\ldots O}$ > 2.73Å) [30]. Weak C-H… O interactions involving the H7, H8A, H9B and H16A atoms. These interactions participate in maintaining the crystalline structure of the compound with an average donor-acceptor distance value of 3.30 Å.

The DFT approach was used for the geometric optimization of **BD(NO$_3$)$_2$** structure and represented in Fig.2. The optimized structural parameters (bond distances and angles) of **BD(NO$_3$)$_2$** were obtained using the B3LYP/6−311++G** method. The results obtained are compared with the crystallographic data determined by XRD. Inspection of Table S1 shows that a relatively small difference between the calculated values and the values deduced from the X-ray experiment. The deviation of the theoretical values from the XRD ones is explained by the fact that deviation of theoretical values from experimental ones is elucidated by the fact measured in crystalline phase. The lengths of N25−O27 and N29−O32 bonds varying from 1.26 Å (exp) to 1.30 Å (theo), confirm the deprotonation in nitrate anions. On the other hand, the protonation of the N1 and N21 atoms of 1,3-Benzenedimethanaminium cation was confirmed by the lengthening of the C5−N1 and C18−N21 distances. Indeed, the N−H bonds involved in N−H ... O hydrogen bonds are lengthened by 0.2 Å. In conclusion, the B3LYP method anticipates geometric parameters, which are much nearer to the experimental data.

3.2. HS analysis

In order to obtain visualization of intermolecular contacts in **BD(NO$_3$)$_2$**, HS analysis was carried out. Both the 3D HS and 2D fingerprint plots are unique for each molecule/ion constituting the asymmetric unit of a crystal structure. HS was represented by d_e and d_i, which denote, respectively, the distance from the nearest atom outside and inside of the surface and both are used to define the normalized contact distance (d_{norm}). They offer an easy way of comparing intermolecular contacts to vd radii. The normalized distance (d_{norm}) can be defined and calculated as a function of d_e, d_i and the vdW radii of the suitable atoms internal and external to the surface via this following expression:

$$\boldsymbol{d_{norm} = \frac{d_i - r_i^{vdW}}{r_i^{vdW}} + \frac{d_e - r_e^{vdW}}{r_e^{vdW}}}$$

Fig. 3 illustrates the HS and the intermolecular contacts of the studied molecule mapped over d_{norm} (-6.00−1454) (Fig. 3a) and d_e (0.743−2.646 Å) (Fig. 3b). For the visualization of d_{norm}, a red−blue−white (RBW) color scale was selected, red zones (lengths lower than sum of vdW radii), white zones (the distance of contact which is exactly the vdW partition), and blue zones (lengths high than sum of vdW radii). The red zones demonstrate the important N(C)−H…O hydrogen bonding among ammonium group and nitrate anion, on the other hand the white and blue zones correspond respectively to the C… H, H… H and N…H interactions. Concerning the

d_e mapping the network of hydrogen bonds occupies well-defined orange zones; the H ... H, N ... H and C ... H contacts are located at the level of weak blue spots.

The quantitative results of the HS analysis are illustrated in Fig. 4; this figure contains the percentages of contributions for a contacts and atoms variety in the crystal structure. The combination of d_e and d_i in the two-dimensional fingerprint plot provides a summary of the intermolecular contacts exist in our crystal, so the fingerprint plots of which the most important are C… H / H… C and O… H / H… O, H… H presented in Fig. S3. The O ... H / H ... O interactions (Fig. S3a) are predominant, they participate with 62.8% of the total surface of Hirhfeld, and these contacts appear in the form of two distinct symmetrical points with a sum $d_e + d_i \sim 1.8$ Å, this value is less than the sum of the vdW radii of the hydrogen (1.09Å) and oxygen (1.52Å) atoms. These contacts correspond to the N−H… O and C−H… O hydrogen bonds. Note that H… O and H… O interactions proportions are not similar (O… H (32.8%) and H… O (30%)). The area of H… H interactions (20.2%) (Fig. S3b) appears as a large region of the fingerprint plot with a highest concentration in the central region, shown in light blue, with $d_e = d_i \sim 1.3$ Å. The sum of the components d_e and d_i is greater than the sum of the vdW radii of the hydrogen atoms. Finally, the C… H / H… C contacts show on its 2D graph (Fig. S3c) the presence of two wings centered on a sum $d_e + d_i \sim 2.6$ Å (this sum is less than the sum of the vdW radii of the carbon: 1.70 Å and hydrogen: 1.09 Å atoms) with a 12% stake on the HS.

Supplementary examination of HS was supervised using a novel descriptor, the enrichment report (ER), which is designated as the fraction of the percentage of actual contacts in the crystal to the computed percentage of random contacts. All the enrichment ratios (ER) of intermolecular contacts involved in the asymmetric unit of **BD(NO$_3$)$_2$** are tabulated in Table S3. The list of ER highlights the O… H / H… O contacts ($ER_{OH} = 1.58$) which appear to be favored in the crystal packaging with the formation of N(C)−H… O hydrogen bonds. The H...H, N…O and N...H contacts are, respectively, slightly enriched and disfavored ($E_{HH} = 0.59$, $E_{NO} = 1.05$ and $E_{NH} = 0.96$). On the other hand, H…C contacts are favored in a sample of C−H aromatic molecules with an average E_{HC} value of 1.71.

3.3. Frontier Molecular Orbital's

The theory of frontier molecular orbitals explains the formation of molecular orbital's of the HOMO and LUMO type. These two forms of orbit play a main position in the covalent chemical bond, in particular in the formation of the π bond. As an essential difference between HOMO and LUMO, we can say that HOMO can donate electrons while LUMO can receive electrons. In addition, the presence of HOMO is characteristic of nucleophiles, while the presence of LUMO is characteristic of electrophiles. The $E_{LUMO}-E_{HOMO}$ is defined as the gap energy (Eg). This quantity of Eg is used to characterize the kinetic stability and the chemical reactivity of the compound. A high value of Eg indicates a great stability of the compound. whereas, a low value of Eg is a criterion of high reactivity. The HOMO and LUMO border orbitals involved in the electronic transitions of the **BD(NO_3)$_2$** compound, are visualized in Fig. S4. The Eg (Eg =$E_{LUMO}-E_{HOMO}$) is in the environs of 4.36 eV, this elevated value suggests a high kinetic stability and a little chemical reactivity. Starting from the of the HOMO and LUMO energies, chemical parameters of the studied molecule such as electronegativity χ, chemical potential μ, electronic affinity A, hardness η(A hard molecule has a large Eg), softness S (A soft molecule has a low Eg)and electrophilic index ψ(A good nucleophile is characterized by weak ψ, and vice versa), are calculated and tabulated in Table 2. Before continuing, let's remember the following concepts:

According to Table 2 gathering the various chemical parameters, the electrophilic index Ψ is equal to 3.19 eV, this value is relatively high, this allows us to conclude that **BD(NO_3)$_2$** considered as a good electrophile. The chemical potential is less than zero (μ = -4.10), this indicates that **BD(NO_3)$_2$** is steady, does not deteriorate spontaneously into its elements, therefore it is biologically active [31]. Usually these parameters are similar to those found in other organic nitrate [4,5].

3.4. AIM topological and molecular electrical potential surface

The AIM theory provides a significant amount of information to better understand the nature of the revealed NCI including H-bonds, therefore R. Bader proposed this topological approach (AIM) which considers the electron density ρ(r) as a local function of the molecular system. Besides, the Laplacian of the electron density $\nabla^2\rho(r)$ at the CP point is a potent tool in the classification of binding zones. Areas of charge concentration are characterized by $\nabla^2\rho(r) < 0$ and those of charge depletion have $\nabla^2\rho(r) > 0$. According to AIM theory, a chemical bond is characterized by the existence of a BCP. Bader's theory also makes it possible to distinguish the nature of the interatomic interaction between two atoms involved, the electronic structure, the non-binding interactions and the chemical reactivity of the studied compound, from the different energy properties (the densities of kinetic energy G, potential V and total H = G + V) and bond energy E_{bond}= V(r)/2. According to criterion of Rozas et al. [32], H- bonds can be classify into 3 categories: we have strong H-bonds if the $\nabla^2\rho(r) < 0$ and total energy densities (H(r)) < 0; moderate H-bonds if $\nabla^2\rho(r) > 0$ and H(r) < 0 and weak H-Bonds if $\nabla^2\rho(r) > 0$ and H(r) > 0.

The graphical representation of AIM analysis of BD(NO_3)$_2$ is given in Fig. S5 while the corresponding topological parameters are presented in Table 3. The examination of this table shows that at BCPs located at the O ··· H bonds, the electron densities are 0.03, 0.0120, 0.0061, 0.0203 and 0.0178 u.a with laplacian values of 0.1008, 0.0418 and 0.0219, 0.0787 and 0.0594. These positive values of the $\nabla^2\rho(r)$ indicate depletion of electronic charge along the binding path. The G/ρ ratio is used to distinguish the type of interaction. This ratio must be greater than 1.0 in the case of H-bonding. In the present work, this ratio is equal to 0.8 for H2 ... O32 and 0.82 for H4 ... O28, close to 1.0 which characterizes the presence of a hydrogen bond. Similar results, for other compounds [33], having a ratio slightly less than 1.0 confirmed the presence of a weak hydrogen bond. According to the Rozas et al. criterion $\nabla^2\rho$ (r)> 0 and H (r)> 0, this allows us to conclude that H-bond is classified as weak.

The surface area of MEP is used to predict the reactivity of molecules. It is very helpful for the qualitative interpretation of electrophilic and nucleophilic reactions and hydrogen bond interactions. Its importance lies because it displays numerous molecular properties namely the positive, negative and neutral regions of MEPS in terms of a color code. The color blue indicates the strong attraction while the red shows a region of strong repulsion and the green indicates the neutral zone. To predict the reactive sites for electrophilic and nucleophilic attack for the **BD(NO_3)$_2$** compound the MEP is computed at level B3LYP/6–31++G** using the Gauss view software and illustrated in Fig. S6. However, it can be seen from this figure that negative electrostatic potential (EP) is more localized on the oxygen atoms which is indicated by a red spot, the positive EP is localized on the ammonium group, therefore the electrophilic site (deficient in electrons) is found (dark blue) at the level of the hydrogen atom of ammonium group while the nucleophilic site is observed (dark red) at the level of the oxygen atom of nitrate group. This shows clearly the existence of N−H ⋯ O intermolecular interaction. These results clearly explain the formation of H-bonds in the studied compound and its important role in its stabilization.

3.5. RDG and isosurface analyses

To corroborate and confirm the results obtained from the AIM analysis, the analysis of multi-wave functions was performed by RDG graph and isosurface examination of interactions. This is an approach proposed by Johnson et al. [34] to study weak contacts in real space. The RDG is a dimensionless quantity coming from the density and its first derivative:

$$RDG(r) = \frac{1}{2(3\pi^2)^{1/3}} \frac{|\nabla\rho(r)|}{\rho(r)^{4/3}}$$

The different plots and results attained alongside this computational study according to a very precise color code are created respectively by means of the Multiwfn and VMD programs and represented in Fig. 5. In order to understand the nature of the different interactions existing in **BD(NO_3)$_2$**, the density ρ(r) against sign λ_2 was represented. So, if $\lambda_2 < 0$ Attractive and binding interactions (H-bonds), $\lambda_2 > 0$ repulsive and non-binding interactions (steric effect) and the values close to zero representing vdW interactions. The RDG plot (Fig. 5a) shows the enormous solidity of **BD(NO$_3$)$_2$** assured by strong N−H ... O and weak C−H ... O hydrogen bonds. These commitments appeared with a sign λ_2 ρ varing from -0.02 to -0.005 Å. Regarding Fig. 5b, the interactions appear as green plaques are ascribed to the vdW interactions; its plates are situated precisely among the hydrogen atoms. The elliptical red plate presented in the middle of the benzene nucleus is associated to repulsive interactions that illustrate a strong steric result. Finally the blue spot existing among the hydrogen and oxygen atoms suggests the strong attractive interaction N−H ... O.

3.6. Thermal analysis

The differential and thermogravimetric thermal analysis curves of **BD(NO$_3$)$_2$** on a sample (m = 18.62 mg) carried out a temperature interval [298−773 K] are shown in Fig. S7a. The DTA curve detects an endothermic peak around 441 K, not including loss of mass which agree with the melting of **BD(NO$_3$)$_2$**. This occurrence is additional established by the heating of our composite on a Kofler bench.This later, makes it probable to approximate the melting point of a material, this temperature (444 K) is close to that detected on the DTA curve. A second exothermic peak observed at 525 K accompanied by a significant loss of mass during which our compound undergoes total decomposition which leads to volatile gases (NO_2, NO) and a black carbon residue.

The calorimetric thermal study carried out under argon on **BD(NO$_3$)$_2$** compound heated from room temperature to 573 K at a speed of 5 K.min^{-1}, shows on the curve obtained (Fig.S7b) two peaks one endothermic located at 439 K and the other exothermic at 510 K corresponding respectively to the melting and decomposition of **BD(NO$_3$)$_2$**. These two phenomena are also observed by DTA / TG. The peak located at 441 K, corresponding to the melting of the compound, is accompanied by a heat of transformation: ΔH_{fusion} = 25.79 kJ.mol^{-1}.

3.6. Electrical behavior

The electrical conductivity of synthesized compound **BD(NO$_3$)$_2$** has been determined by the complex impedance method as a function of temperature and over a wide frequency range of 0.01−13000 kHz. The values of conductivity of the produced compound are grouped together in Table S4. The conductivity is determined from the equation $\sigma = \frac{e}{SR}$ where e, S and R represent the thickness, area and resistance of the sample used, respectively. The polycrystalline **BD(NO$_3$)$_2$** was pressed into pellet with a diameter of 13 mm and a thickness of 1.25 mm using a hydraulic press of 7 tons.

- Impedance spectroscopy

The conductivity measurement of **BD(NO$_3$)$_2$** compound was performed by the complex impedance method. The resistance (R) values are determined from the intersection of the Nyquist diagram with the x-axis as shown in Fig. 6a. This figure represents by way of example the curves reflecting the variation of –Z'' as a function of f (Z') at different temperatures, indicating that resistance of the sample studied decreases as a function of temperature. The shape of the impedance diagrams is presented as semicircles centered under the real axis and passing near the origin characterize the two contributions of grains and grain boundaries, suggesting the departure of the ideal Debye behavior [35]. This behavior is similar to that observed in semiconductor materials [36]. We respectively represent the variation of the real part of the impedance Z' and of the imaginary part Z'' at different temperatures as a function of frequency. Indeed, Fig. 6b (Z'= f (logf)) shows that Z' decreases when the temperature and frequency increase. Note in Fig. 6c, which represents Z'' = f (logf), the appearance of peaks (ω_{max}, Z''_{max}) whose intensity decreases with increasing temperature. These peaks reflect the presence of relaxation phenomenon. It is observed that each peak is centered at a maximum frequency (f_{max}) and shifts towards the high frequencies for increasing temperatures. This explains why the relaxation phenomenon depends on the temperature.

- Electrical modulus

The complex modulus formalism is a very important and practical tool for complex impedance spectroscopy to determine and interpret the dynamic aspects of electrical transport phenomena (charge carrier jump speed, relaxation time, etc.). Macedo et al. [37] were the first to use the complex modulus formalism (**$M^* = j\omega c_0 Z^* = M' + jM''$**) ($\omega$ = angular frequency, C_0 = geometric capacity) to analyze the relaxation of conductivity in glasses and in highly concentrated aqueous solutions. The calculation of the two sides real and imaginary is obtained using the following formulas: **$M' = -\omega c_0 Z''$; $M'' = \omega c_0 Z'$** with $C_0 = \frac{\varepsilon_0 S}{e}$ ($\varepsilon_0$is the permittivity of free space). Fig. 7a represents the frequency response M' at different temperatures, this curve is characterized in the low frequency region by a very low value M' close to zero indicating that the polarization phenomena due to the interfacial effects and to the electrodes have a negligible contribution. By increasing the frequency, M′ gradually increases it reaches a maximum in the high frequency region ($M'_\infty = 1 / \varepsilon_\infty$). The variation of the imaginary part M'' as a function of the frequency at different temperatures is represented in Fig. 7b. M'' is characterized by values very close to zero at low frequency, by increasing the frequency the spectra of the sample increase until reaching maxima at a noted frequency (f_{max}) highlighting the relaxation phenomenon of the systems. Knowing the value of f_{max} makes it possible to calculate the relaxation time (τ) by applying the following formula: $\tau = 1 / 2\pi f_{max}$. The peaks positions tend to shift towards high frequencies as the temperature increases. This systematic shift means that f_{max} increases as the temperature is raised, indicating a decrease in the relaxation time as a result of thermal activation of the charge carriers. The low frequency region of the imaginary part represents the part in which the charge carriers are mobile at long lengths where the migration of these ions occurs by hopping between neighboring sites. In the high frequency region, charge carriers have been spatially confined in their potential wells [38].

- Electrical permittivity

The permittivity notion of a material medium is linked to polarization phenomena where (ε) is represented by: $\varepsilon^* = \varepsilon' + i\varepsilon''$. The real part ε' designates the capacity of the dielectric to store electrical energy while the imaginary part ε" materializes the dielectric losses due to polarization and ionic conduction [37]. ε' (ω) and ε" (ω) are given by:

$$\boldsymbol{\varepsilon'(\omega) = \frac{1}{\omega\ C0}\frac{-Z''}{Z'^2+Z''^2}\ ;\ \varepsilon''(\omega) = \frac{1}{\omega\ C0}\frac{Z'}{Z'^2+Z''^2}}$$

Fig. 7c illustrates the variation of the dielectric constant ε′ as a function of frequency and temperature. Qualitative analysis of the different curves for the compound produced shows that ε′ is characterized by a large contribution at low frequencies then decreases sharply to reach constant values at higher frequencies. This dielectric dispersion can be explained by the phenomenon of dielectric polarization. In the low frequency region, all the polarization phenomena (electronic, ionic and dipolar) are present, since all the charges can follow the variations of the applied field. In addition, the presence of the interfacial polarization or Maxwell effect- Wagner: Under the effect of the electric field, the charge carriers migrate inside the material and tend to concentrate around defects such as vacancies and grain boundaries presenting a large contribution to ε′ [38]. As the frequency increases, the contribution of each type of polarization gradually disappears. Also the formed dipoles have more difficulty in following the variations of the applied field which become more and more rapid. This difficulty is greater the greater the mass of the charged particle. Thus charges of smaller mass can polarize up to high frequencies, while charges of greater mass can only polarize at low frequencies. We also see that ε′ increases with increasing temperature following thermal activation of electric charge carriers. Concerning the variation of ε" as a function of the frequency at different temperatures, it is represented in Fig. 7d. It can be seen that ε" decreases rapidly at low frequencies to reach very low values at high frequency. It can be seen that ε" decreases rapidly at low frequencies to reach very low values at high frequencies. The dispersion of ε " may be due to the contribution of distinct effects such as direct current conductivity and the superposition of different polarizations types (interfacial polarization and dipole orientation) [40]. This type of frequency dependence of ε''(ω) is typically associated with conduction losses [41]. As the frequency increases, the orientation of the dipoles cannot follow the rapid oscillation of the applied electric field. This phase shift causes the reduction of various types of polarizations until their disappearance, which explains the decrease in the permittivity ε'' as the frequency increases [40,41].

- Conductivity analysis

Fig. S8 shows the conductivity evolution in as a function of inverse of the temperature (Log (σ.T) = f (1000 / T)) for **$BD(NO_3)_2$** compound. This curve consists of a linear branch which does not show any break, it is in good agreement with Arrhenius' law:

$$\boldsymbol{\sigma T = A\exp(-E_a/KT)}$$

Where **A** is a constant depending on the material, **T** is the absolute temperature in Kelvin, **K** is Boltzman's constant and **E_a** is the activation energy of the species responsible for conductivity. The examination of this curve demonstrate a single mode of conduction with an activation energy E_a equal to 0.18eV in the temperature range studied (343-393 K). The conductivity results are confirmed by the thermal study. This later shows that there are no thermal accident in this range of temperature. It can be noticed that the conductivity increases to a value equal to $4.61.10^{-6}\ \Omega^{-1}cm^{-1}$, this significant variation probably die the high mobility of the H^+ protons under the effect of thermal agitation, as well as the appearance of new dipole-dipole charge carriers that improve conductivity within our material. The comparison of the value of activation energy (Ea = 0.18eV) and conductivity [$1.33.10^{-6}\ \Omega^{-1}cm^{-1}$ (343 K) to $4.61.10^{-6}\ \Omega^{-1}cm^{-1}$ (393 K)] with those of other materials in the bibliography [36] shows that **$BD(NO_3)_2$** material is indexed among semiconductors.

3.7. Vibrational behavior

The synthesized compound, optimized with C_1 symmetry, was further characterized by infrared absorption spectroscopy. The infrared spectrum of **$BD(NO_3)_2$** measured in the solid phase between 4000 and 400 cm^{-1} and recorded at room temperature is shown in Fig. 8 compared with the corresponding predicted for the monomer and its dimer in gas phase by using the B3LYP/6-311++G(d,p) method. This study allowed us to determine its vibrational characteristics by attributing the observed frequencies to the different types of vibratory movements in the different polyatomic groups. A very important fact is that two intense bands predicted in the monomer by B3LYP/6-311++G(d,p) calculations at 2265 and 1942 cm^{-1} and assigned respectively to N-H···O-N stretching modes between both NH_3 and NO_2 groups are not observed in the experimental IR spectrum. Hence, the presence of dimer justifies the absence of those bands in the experimental spectrum because those bands are observed with reduced intensities and shifted toward higher wavenumbers in its infrared and Raman spectra. We observed that the theoretical spectra is different from the experimental ones because the theoretical calculations are performed in the gas phase while the experimental ones are obtained in the solid phase where the crystalline packing forces are important and the shapes of the bands are wider and have greater intensities. For these reasons, the complete assignments of bands observed in the experimental IR spectrum were performed taking into account the SQMFF methodology and the corresponding normal internal coordinates [25]. With this methodology, the force constants calculated from the Molvib program are multiplied by scale factors until the theoretical frequencies are reproduced as best as possible to the experimental ones [26]. In this trioxonitrate species are expected 90 vibration normal modes having all modes activities in both infrared and Raman spectra due to the C_1 symmetry. The predicted Raman spectra of monomer and dimer are given in Fig. S9. The theoretical Raman spectra predicted for monomer and dimer in activities were corrected to intensities by using known equations [42,43]. Particularly, the internal vibration modes of the NH_3^+ groups were considered with C_{3V} symmetry while the corresponding to NO_3^- anion with symmetry D_{3h}, as have been widely published in the literature [3-5, 9,27,36]. In Table S5 are summarized observed and calculated wavenumbers (cm^{-1}) and assignments for **BD(NO$_3$)$_2$** in gas phase by using the B3LYP/6-311++G** method. The vibrational assignments were performed taking into account the potential energy distribution (PED) contributions. Here, we have considered in some cases PED contributions < 10%, as observed in Table S5, especially in the region of lower wavenumbers where some vibration modes are coupled among them. Here, the assignments for the most important groups are discussed by regions below.

Assignments

4000-2000 cm^{-1} region. The assignments of vibrations modes to the observed bands in the IR spectrum (Fig.16) of 1,3-Benzenedimethanaminium cation were made by the SQM calculations performed here and, by comparison with similar reported in the literature [8, 26]. In this region the expected vibration modes are quickly assigned because they are predicted as modes practically pure (PED equal to 99 %). Thus, in this region six stretching modes are expected for the two NH_3^+ groups and, where two asymmetric $\nu_a(NH_3^+)$ stretching modes are assigned to the IR bands at 3375 and 3319 cm^{-1} while the other two asymmetric modes are forming H bonds (N-H···O-N) with the NO_3^- groups and, for these reasons, they are shifted to lower wavenumbers at 2175 and 1867 cm^{-1}[44]. Hence, the weak IR bands at 2153 and 1759 cm^{-1} are assigned respectively to the $\nu_a(NH_3^+)$ stretching modes. The corresponding symmetric modes are assigned as predict the calculations to the strong IR bands at 3252 and 3180 cm^{-1}. Other vibration modes assigned in this region are the C-H stretching and the symmetric and asymmetric CH_2 stretching modes. Here, the symmetries of these modes were not confirmed because the experimental Raman spectrum was not recorded. As was previously mentioned, the presence of dimeric species justify the low intensities of bands observed in the experimental IR spectrum of asymmetric NH_3^+ stretching modes assigned to the N-H···O-N bonds formed between both NH_3^+ and NO_3^- groups.

2000-1000 cm^{-1} region. The asymmetric deformation modes $\delta_{as}(NH_3^+)$ are expected in the 1600-1575 cm^{-1} region while the corresponding symmetric $\delta_s(NH_3^+)$ around 1500 cm^{-1} [27,45]. Some vibration modes (NH_3·deformation and rocking modes) were predicted by calculations coupled among them and, for these reasons, these modes are calculated with low PEDs contributions (6-8 %). Thus, these modes are assigned to the observed IR bands between 1623 and 1516 cm^{-1}. The stretching modes ν(C=C) of the phenyl group were assigned at 1623 and 1596 cm^{-1} while the deformation modes of the CH_2 groups, observed experimentally in the region between 1560 and 1035 cm^{-1}, are assigned to the bands between 1464 and 1417 cm^{-1}. The in-plane C-H deformation vibrations are assigned in the spectral range from 1361 to 1163 cm^{-1}, as predicted by SQM calculations (28-12% PED). Also, in this region are predict at 1316 and 1232 cm^{-1} some C-C stretching modes with partial double bond character, hence, these modes can be assigned to the IR bands observed in this region.

Here, each NO_3^- groups is analyzed as two N=O (NO_2) and one N-O stretching modes, thus, the asymmetric stretching modes $\nu_{as}(NO_2)$ are predict by SQM calculations (62 and 15% PED) at 1463 and 1426 cm^{-1} and, for these reasons, the IR bands at 1516 and 1361 cm^{-1} are easily assigned to these vibration modes. The corresponding symmetrical stretching modes ν_sNO_2 are assigned to the band located in the IR spectrum at 1183 cm^{-1} because both are predict by SQM calculations (34-22 %PED) at 1216 and 1194 cm^{-1}.

The rocking modes of NH_3^+ groups are also predicted in this region with low PED contribution (17-8 %), thus, the bands between 1129 and 1041 cm^{-1} can be assigned to these vibration modes.

1000-10 cm^{-1} region. In this region the IR band of medium intensity at 996 cm^{-1} can be assigned to the N25-O27 and νN29-O32 stretching modes (PED 56 and 22%) while wagging, rocking and deformation modes of NO_2 groups are assigned as predicted (PED between 93 and 27%) respectively at 820/813, 730/726 and 711/708 cm^{-1}. Note that in Table S5 only the vibration modes were assigned to the IR bands until 465 cm^{-1} because the IR spectrum was recorded from 4000 to 400 cm^{-1}.

3.8. Force fields

The scaled force constants for **$BD(NO_3)_2$** in gas phase by using the B3LYP/6-311++G(d,p) method are presented in Table 4 compared with reported for *p*-Xylylenediaminium bis(nitrate), 1-buthyl-3-methyl imidazolium nitrate and 2-(4-nitrophenyl)-4H-3,1-benzoxazin-4-one at the same level of theory [27,46]. These parameters were calculated from the harmonic force field computed with the SQMFF methodology and the Molvib program [25,26]. First of all, analyzing the $f(\nu NH_3)$ force constants for the two compared species we observed that for $BD(NO_3)_2$ the value is higher than the corresponding to *p*-Xylylenediaminium bis(nitrate) [27] probably due to that in this compound there are two NH_3 groups while in the compared compound an N-H bond is linked to two O atoms of only one NO_3^- group. On the other hand, the $f(\nu NO_2)$ force constant presents higher value in *p*-Xylylenediaminium bis(nitrate) because the nitrate group is linked only to one NH_3^+ group and, for the same reason, the $f(\nu N\text{-}O)$ force constant has a higher value in $BD(NO_3)_2$. In 2-(4-nitrophenyl)-4H-3,1-benzoxazin-4-one, the $f(\nu NO_2)$ force constant is comparable to the predicted for *p*-Xylylenediaminium bis(nitrate) while the $f(\nu N\text{-}O)$ force constant has higher value in the ionic liquid probably due to the interaction of N-O bond with H atoms of C-H of ring belonging to 1-buthyl-3-methyl imidazolium cation. The $f(\nu C\text{-}N)$ force constant is higher in 2-(4-nitrophenyl)-4H-3,1-benzoxazin-4-one while the $f(\nu C\text{-}C_R)$ force constant has a higher value in the ionic liquid. The other constants have approximately similar values.

3.9. Molecular docking analysis

In order to interpret the biological activity of studied compounds, the molecular docking was used to determine a new drug conception. This technique is a powerful tool to identify the best orientation between ligand-protein binding sites. Furthermore, it supports the partnership between the theoretical and pharmaceutics research and reduces the time to carry out the syntheses of new medicaments. The **$BD(NO_3)_2$** compound was chosen to be docked with various fungia and bacteria proteins. A Xylylenediamine and its derivates highly used in pharmaceutical owing to its antimicrobial activity [8]. In fact, the fungi (*Aspergillus niger*, *Aspergillus flavus*, *Aspergillus fumigates* and *Penicillium sp.)* and the bacteria (*Escherichia coli*, *Klebsiella pneumonia*, *Staphylococcus epidermidis* and *Bacillus subtilis*) docking activity has been tested for various proteins during a bibliographic study. These fungi are well known in asthmatic diseases and can grow in the sinuses. In addition, these bacteria are responsible for infections in the urinary tract. In this work, four fungal enzymes such as 5HWC, 3K4Q, 1XY3, 4LEB and 1TG7 and four bacteria enzymes 6GCV, 4IIT, 6WVK and 5TU9 were chosen and docked with the ligand **$BD(NO_3)_2$**. The best post docked of our compound with the various proteins was carried out by using iGEMDOCK program [22]. During the docking calculation we obtained 10 poses, which we only present the best pose that is relating to minimal energies (Figs. 9 and S10). The results of docking calculations (Total energy, vdW, H-bond, Electronic, AverConPair) are summarized in Table 5. Note that the total energy is the sum of vdW, H-bond and electronic binding interaction. The docking scores indicate that the fungal protein 3K4Q has the highest total energy equal to -99.65 kcal.mol^{-1}. In addition, she has the largest vdW interaction (-65.51 kcal.mol^{-1}), but the strongest value of H-bond (-37.41 kcal.mol^{-1}). The 1XY3 has the weakest binding fungal, but it has the highest H-bond value compared to 4LEB and 5HWC. For bacteria, the 6GCV has the great value of total energy equal to -93.53 kcal.mol^{-1}and she has also the highest value of H-bond (-46.33 kcal.mol^{-1}). While, 5TU9 has the weakest total energy and also it forms the strongest H-bond and electronic binding interaction equal to -25.60 kcal.mol^{-1} and 0.59 kcal/mol respectively. Same also for 4IIT and 1XK9 whose total energy equal to -85.98 kcal.mol^{-1} and -84.06 kcal.mol^{-1} respectively. In Fig. 10, we present different forms of intermolecular interactions between **BD(NO$_3$)$_2$** ligand and fungal enzymes 5HWC, 3K4Q, 1XY3, 4LEB and 1TG7. In addition, Fig. S11 represents the interactions between ligand and bacteria protein 6GCV, 4IIT, 6WVK and 5TU9. This figure shows the existence of pi-anion and pi-alkyl interactions between the aromatic group and other alkyl group. Note that the great number of pi-anion and pi-alkyl interactions that involve charge transfer helps to intercalate the drug in the receptor binding site [7]. It is being noticed also the existence of pi-pi interactions, these latter are essential in biological events such as protein-ligand recognition [8]. Also, they can explain the stability of the compound with protein. According to these results, molecular docking indicates that our compounds have a good antimicrobial activity. So, it performs an important role in biological investigations intended on finding and developing new drug of antiproliferative agents. Finally, we can conclude that this compound can be investigated as a powerful inhibitor against these bacteria and fungi.

4. Conclusion

The structural discussion by X-ray diffraction shows that BD(NO$_3$)$_2$ crystallizes in the monoclinic crystal system (P2$_1$/c) with a consolidated and stabilized molecular arrangement by the association of $R_1^2(4)$, $R_4^2(8)$, $R_6^4(14)$, and $\mathrm{R}_4^3(10)$ units forming a three-dimensional network. Theoretical analysis performed by DFT supported the experimental results. The quantitative analysis (fingerprint plots) indicated that the H ⋯ O/O ... H interactions are more frequent in the crystalline stacking around 62.8%; these contacts are responsible for the formation of the N−H…O and C−H…O hydrogen bonds. In addition to hydrogen bonds, the

RDG makes it possible to demonstrate the presence of vdW type interactions and the steric effect. The HOMO−LUMO energy difference as well as the chemical potential is respectively of 4.36 eV and -4.10 eV orders indicating that our material has high kinetic stability and biological activity. Complete vibrational assignments of the fundamental modes of the compound have been reported together with the main force constants. The presence of dimeric species is important to explain why the intense bands predicted for the monomer due to N-H···O-N interactions are not observed in the experimental infrared spectrum. The thermal study of the crystal, shows that it undergoes under the effect of temperature a melting around 441 K followed by a total decomposition in the vicinity of 525 K which leads to volatile gases and a black carbon residue. The electrical conduction study allowed us to study the electrical transport properties of **BD(NO$_3$)$_2$** which increases with temperature and frequency. This approach indicates that observed relaxation process is thermally activated. Finally, molecular docking reveals that the title compound could act as an inhibitor against bacteria and fungi.

Author statement

Sofian Gatfaoui: Formal analysis, Writing – original draft.

Noureddine Issaoui: Investigation, Software.

Silvia Antonia Brandán: Methodology, Conceptualization.

Mouna Medimagh: Formal analysis, Writing.

Omar Al-Dossary: Supervision Validation.

Thierry Roisnel: Software.

Houda Marouani: Validation, Writing –review & editing, Supervision.

Aleksandr S. Kazachenko: Conceptualization, Methodology.

Declaration of interests

x
☐The authors declare that they have no known competing financial interests or personal relationships that could have appeared to influence the work reported in this paper.

Funding: This work was supported by the project number (RSP-2021/61), King Saud University, Riyadh, Saudi Arabia. Tunisian National Ministry of Higher Education and Scientific Research and with grants from CIUNT Project Nº 26/D608 (Consejo de Investigaciones, Universidad Nacional de Tucumán). The authors would like to thank Prof. Tom Sundius for his permission to use MOLVIB.

Supplementary data

Supplementary Information: **Table S1-S5 and Figures S1-S11.**

References

[1] L.M. Novena, S.S. Kumar, S. Athimoolam, Improved solubility and bioactivity of theophylline (a bronchodilator drug) through its new nitrate salt analysed by experimental and theoretical approaches, J. Mol. Struct. 1116 (2016) 45–55.

[2] M.C. Daniel, D. Astruc, Gold nanoparticles: assembly, supramolecular chemistry, quantum-size-related properties, and applications toward biology, catalysis, and nanotechnology, Chem. Rev. 104 (2004) 293–346.

[3] S. Gatfaoui, A. Mezni, T. Roisnel, H. Marouani, Synthesis, characterization, Hirshfeld surface analysis and antioxidant activity of a novel organic-inorganic hybrid material 1-methylpiperazine-1, 4-diium bis(nitrate), J. Mol. Struct. 1139 (2017) 52–59.

[4] S. Gatfaoui, A. Sagaama, N. Issaoui, T. Roisnel, H. Marouani, Synthesis, experimental, theoretical study and molecular docking of 1-ethylpiperazine-1,4-diium bis(nitrate), Solid State Sci. 106 (2020) 106326.

[5] S. Gatfaoui, N. Issaoui, T. Roisnel, H. Marouani, Synthesis, experimental and computational study of a non-centrosymmetric material 3-methylbenzylammonium trioxonitrate, J. Mol. Struct. 1225 (2020) 129132.

[6] O. Noureddine, S. Gatfaoui, S. A. Brandán, H. Marouani, N. Issaoui, Structural, docking and spectroscopic studies of a new piperazine derivative, 1-phenylpiperazine-1,4-diium-bis (hydrogen sulfate), J. Mol. Struct. 1202 (2020) 127351.

[7] O. Noureddine, S. Gatfaoui, S. A. Brandán, A. Sagaama, H. Marouani, N. Issaoui, Experimental and DFT studies on the molecular structure, spectroscopic properties,and molecular docking of 4-phenylpiperazine-1-ium dihydrogen phosphate, J. Mol. Struct. 1207 (2020) 127762.

[8] I. Jomaa, O. Noureddine, S. Gatfaoui, N. Issaoui, T. Roisnel, H. Marouani, Experimental computational and in silico analysis of $(C_8H_{14}N_2)_2[CdCl_6]$ compound, J. Mol. Struct. 1213 (2020) 128186.

[9] O. Noureddine, N. Issaoui, S. Gatfaoui, O. A. Dossary, H. Marouani, Quantum chemical calculations, spectroscopic properties and molecular docking studies of a novel piperazine derivative, J. King Saud Univ.Sci.1016 (2020)101334.

[10] N. Agarwal, I. Verma, N. Siddiqui, S. Javeda, Experimental spectroscopic and quantum computational analysis of pyridine-2,6-dicarboxalic acid with molecular docking studies, J. Mol. Struct, 1245,(5) (2021) 131046.

[11] S. Savita, A. Fatima, Km. Garima, Km.Pooja, I. Verma, N. Siddiqui, S. Javed, Experimental spectroscopic, Quantum computational, Hirshfeld surface and molecular docking studies on 3-Pyridinepropionic acid, J. Mol. Struct., 1243, (5) (2021) 130932.

[12] A. Fatima, J. Bhadoria, S. K. Srivastava, I.Verma, N. Siddiqui, S. Javed, Exploration of experimental and theoretical properties of 5,5-dimethyl 3-amino-cyclohex-2-en-1-one (AMINE DIMEDONE) by DFT/TD-DFT with ethanol and DMSO as solvents and molecular docking studies, J. Mol. Liq. 338, (2021) 116551

[13] E. T. Michalson, J. Szmuszkovicz, Medicinal agents incorporating the 1,2-diamine functionality. Progress in drug research, (1989) 135-149.

[14] Bruker, APEX2, SAINT and SADABS, Bruker AXS Inc, Madison, Wisconsin, USA, 2006.

[15] A. Altomare, M.C. Burla, M. Camalli, G.L. Cascarano, C. Giacovazzo, A. Guagliardi, A.G.G. Moliterni, G. Polidori, R. Spagna, J. Appl. Cryst. 32 (1999) 115.

[16] G.M. Sheldrick, Crystal structure refinement with SHELXL, Acta Cryst. C 71 (2015) 3–8.

[17] K. Brandenburg, Diamond Version 2.0 Impact, GbR, Bonn, 1998.

[18] S.K. Wolff, D.J. Grimwood, J.J. McKinnon, D. Jayatilaka, M.A. Spackamn, Crystal Explorer 3.1, University of Westren Australia, Perth, 2013.

[19] M.J. Frisch, et al., GAUSSIAN 09, Revision A.02, Gaussian, Inc., Wallingford, CT, 2009.

[20] R.I. Dennington, T. Keith, J. Millam, GaussView, Version 5.0.8, Semichem. Inc, Shawnee Mission, KS, 2008.

[21] T. Lu, F. Chen, Multiwfn: a multifunctional wavefunction analyzer, J. Comput. Chem. 33 (2012) 580–592.

[22] J.M. Yang, C.C. Chen, GEMDOCK: a generic evolutionary method for molecular docking, Proteins Struct. Funct. Bioinforma. 55 (2004) 288-304.

[23] http://www.rcsb.org/pdb/.

[24] D.S. Visualizer, Accelrys software inc, Discovery Studio Visualizer 2 (2005).

[25] P. Pulay, G. Fogarasi, G. Pongor, J.E. Boggs, A. Vargha, Combination of theoretical ab initio and experimental information to obtain reliable harmonic force constants. Scaled quantum mechanical (QM) force fields for glyoxal, acrolein, butadiene, formaldehyde, and ethylene. J. Am. Chem. Soc. 105 (1983) 7073.

[26] T. Sundius, Scaling of ab initio force fields by MOLVIB, Vib. Spectrosc. 29 (2002) 89-95.

[27] S. Gatfaoui, N. Issaoui, S.A. Brandan, T. Roisnel, H. Marouani, Synthesis and characterization of p-xylylenediaminium bis(nitrate). Effects of the coordination modes of nitrate groups on their structural and vibrational properties, J. Mol. Struct. 1151 (2018) 152–168.

[28] S. Gatfaoui, H. Marouani, T. Roisnel, H. Dhaouadi, Dopaminium nitrate, Acta Cryst. E 70 (2014) o571–o572.

crystal structure and Hirshfeld surface analysis, Acta Cryst. E 72 (2016) 776-779.

[29] J. Janiak, J. Chem. Soc. Dalton Trans. pp. (2000) 3885–3896.

[30] I. D. Brown, Acta Cryst. A32, (1976) 24–31.

[31] M. Salihovic, S. Huseinovic, S. Spirtovic-Halilovic, A. Osmanovic, A. Dedic, Z. Asimovic, D. Zavrsnik, DFT study and biological activity of some methylx-anthines, Bull. Chem. Technol. Bos. Herzeg. 42 (2014) 31–36.

[32] I. Rozas, I. Alkorta, J. Elguero, Behavior of ylides containing N, O, and C atoms as hydrogen bond acceptors, J. Am. Chem. Soc. 122 (2000) 11154–11161.

[33] D.E. Hibbs, J. Overgaard, R.O. Plitz, X–N Charge density analysis of the hydrogen bonding motif in 1-(2-hydroxy-5-nitrophenyl)ethanone, Org. Biomol. Chem. 1 (2003) 1191.

[34] E.R. Johnson, S. Keinan, P. Mori-Sánchez, J. Contreras-García, A.J. Cohen, W. Yang, Revealing Noncovalent Interactions, J. Am. Chem. Soc. 132 (2010) 6498–6506.

[35] J.R. Macdonald, Impedance spectroscopy, Ann. Biomed. Eng. 20 (1992) 289-305.

[36] S. Gatfaoui, N. Issaoui, T. Roisnel, H. Marouani, A proton transfer compound template phenylethylamine: Synthesis, collective experimental and theoretical investigations, J. Mol. Struct. 1191 (2019) 183–196.

[37] P.B. Macedo, C.T. Moynihan, R. Rose, The long time aspects of this correlation function, which are obtainable by bridge techniques at temperatures approaching the glass transition, Phys. Chem. Glas. 13 (1972) 171-176.

[38] Y. Fujishiro, H. Ito, T. Sato, A. Okuwaki, Synthesis of monodispersed $LaPO_4$ particles using the hydrothermal reaction of an $La(edta)^-$ chelate precursor and phosphate ions, J. Alloys Compd. 252 (1997) 103-109.

[39] J. Maxwell, A Treatise on Electricity and Magnetism, 1, Oxford Univ. Press, (1873) 328.

[40] Y. Xi, Y. Bin, C.K. Chiang, M. Matsuo, Dielectric effects on positive temperature coefficient composites of polyethylene and short carbon fibers, Carbon 45 (2007) 1302-1309.

[41] S. VinothRathan, G. Govindaraj, Thermal and electrical relaxation studies in $Li_{(4+x)}Ti_xNb_{1-x}P_3O_{12}$ ($0.0 \leq x \leq 1.0$) phosphate glasses, Solid State Sci. 12 (2010) 730-735.

[42] G. Keresztury, S. Holly, G. Besenyei, J. Varga, A.Y. Wang, J.R. Durig, Vibrational spectra of monothiocarbamates-II. IR and Raman spectra, vibrational assignment, conformational analysis and ab initio calculations of S-methyl-N,Ndimethylthiocarbamate, Spectrochim. Acta 49 (1993) 2007-2026.

[43] D. Michalska, Wysokinski, The prediction of Raman spectra of platinum(II) anticancer drugs by density functional theory, chem. phys. letters 403 (2005) 211-217.

[44] N. Issaoui, N. Rekik, B. Oujia, M.J. Wojcik, Anharmonic effects on theoretical IR line shapes of medium strong H(D) bonds, Int. J. of Quant. Chemistry, 109 (2008) 483-499.

[45] S. Trabelsi, N. Issaoui, S. A. Brandán, F. Bardak, T. Roisnel, A. Atac, H. Marouani, Synthesis and physic-chemical properties of a novel chromate compound with potential biological applications, bis(2-phenylethylammonium) chromate(VI), J. Mol. Struct.1185 (2019) 168-182.

[46] J. Kausteklis, V. Aleksa, M. A. Iramain, S. A. Brandán, Effect of cation-anion interactions on the structural and vibrational properties of 1-buthyl-3-methyl imidazolium nitrate ionic liquid, J. Mol. Struct. 1164 (2018) 563-576.

Table captions

Table 1. Crystal data and experimental parameters used for the intensity data collection strategy and final results of the structure determination.

Table 2. Calculated energy value for the studied compound by using TD-B3LYP/6-311++G(d,p) method.

Table 3. Topological parameters of $BD(NO_3)_2$ compound calculated at DFT/B3LYP/6-311++G(d,p).

Table 4. Comparison of main scaled internal force constants for **$BD(NO_3)_2$** in gas phase by using the B3LYP/6-311++G(d,p) method with reported for similar species at the same level of theory.

Table 5. Results of docking calculations (Total energy, VDW, H-bond, Electronic, AverConPair).

Table 1

CCDC	2062160
Empirical formula	$C_8 H_{14}N_2(NO_3)_2$
Temperature	150 K
Formula weight (g mol^{-1})	262.23
Crystal system	Monoclinic
Space group	$P2_1/c$
a, b, c (Å)	21.4308 (7), 5.7255 (2), 20.4476 (5)
β (°)	108.502 (1)
Z	8
V(Å^3)	2379.28 (13)
F(000)	1104
Radiation type	Mo Kα
μ(mm^{-1})	0.13
Crystal size (mm)	0.47 x 0.24 x 0.17
Independent reflections	5457
Reflections with $I > 2\sigma(I)$	4429
R_{int}	0.036
Diffractometer	Bruker APEXII
Absorption correction	Multi-scan
T_{min}, T_{max}	0.889, 0.979
Refined parameters	329
$R[F^2 > 2\sigma(F^2)]$	0.047
$wR(F^2)$	0.129
Goodness of fit	1.04
$\Delta\rho_{max}$, $\Delta\rho_{min}$ (eÅ^{-3})	0.51, -0.28

Table 2

E_{HOMO}(eV)	-6.2839
E_{LUMO}(eV)	-1.9352
$\Delta E_{LUMO\text{-}HOMO}$(eV)	4.3487
Electronic affinity A (eV)	1.9352
Ionization potential I (eV)	6.2839
Chemical hardness η (eV)	2.1743
Softness S (eV)	0.4599
Chemical potentiel μ (eV)	-4.1095
Electronecativity χ (eV)	4.1095
Electrophilicity ψ (eV)	3.1937

Table 3

Bond critical points	**ρ(r) (u.a)**	**$\nabla^2\rho(r)$ (u.a)**	**V(r) (u.a)**	**G(r) (u.a)**	**H(r) (u.a)**	**E_{int} ($kJ.mol^{-1}$)**	**G(r)/ρ(r)**
$C_9 \ldots O_{32}-N_{29}$	0.0027	0.0096	-0.0013	0.0018	0.0005	-1.64	0.67
$H_2 \ldots O_{32}-N_{29}$	0.0300	0.1008	-0.0229	0.0240	0.0011	-29.83	0.8
$C_{15} \ldots O_{26}-N_{25}$	0.0050	0.0159	-0.0028	0.0033	0.0005	-3.60	0.66
$H_{22} \ldots O_{26}-N_{21}$	0.0120	0.0418	-0.0079	0.0091	0.0012	-10.31	0.76
$C_{16}-H_{17} \ldots O_{27}$	0.0061	0.0219	-0.0038	0.0046	0.0008	-4.95	0.76
$N_1-H_4 \ldots O_{28}$	0.0203	0.0787	-0.0141	0.0168	0.0027	-18.36	0.82
$N_{21}-H_{22} \ldots O_{27}$	0.0178	0.0594	-0.0114	0.0131	0.0017	-14.86	0.73

Table 4

B3LYP/6-311++G**Method				
Force constants	$BD(NO_3)_2$ [a]	2-(4-nitrophenyl)-4H-3,1-benzoxazin-4-one[b]	1-buthyl-3-methyl imidazolium nitrate[c]	p-Xylylenediaminium bis(nitrate)[d]
$f(\nu NH_3)$	5.19			4.36
$f(\nu C\text{-}H)_R$	5.07	5.18	5.14	
$f(\nu NO_2)$	8.37	9.39	8.00	9.74
$f(\nu N\text{-}O)$	6.09		6.50	4.25
$f(\nu CH_2)$	4.86		4.71	
$f(\nu C\text{-}N)$	4.00	7.47	4.35	4.23
$f(\nu C\text{-}C_R)$	6.47	6.24	7.60	6.34
$f(\delta CH_2)$	0.85		0.80	
$f(\delta NH_3)$	0.60			
$f(\delta NO_2)$	1.63		1.60	1.53

Units are mdyn $Å^{-1}$ for stretching and mdyn Å rad^{-2} for angle deformations

[a]This work, [b]From Ref. [44], [c]From Ref. [45], [d]From Ref. [26]

Table 5

ligand		Total energy	VDW	H-bond	Electronic	AverConPair
1,3-Benzenedimethanaminium bis(trioxonitrate)				**Fungi**		
	3K4Q	-99.65	-37.41	-65.51	3.28	22.39
	4LEB	-90.48	-51.72	-37.02	-1.73	26.11
	5HWC	-86.44	-48.16	-37.94	-0.33	21.22
	1XY3	-83.62	-48.33	-38.36	3.06	25.44
				Bacteria		
	6GCV	-93.53	-44.68	-46.33	-2.53	21.78
	4IIT	-85.98	-38.63	-41.58	-5.76	19.33
	1XK9	-84.06	-44.06	-37.13	-2.87	22.89
	5TU9	-72.26	-47.26	-25.60	0.59	19.22

Figure captions

Fig. 1. ORTEP drawing of BD(NO_3)$_2$ with the atom-labeling scheme. Displacement ellipsoids are drawn at the 30% probability level (a). H atoms are represented as small spheres of arbitrary radii. Projection along the $\vec{b}$ axis of atomic arrangement of BD(NO_3)$_2$ (b).

Fig. 2. The optimized structure of BD(NO_3)$_2$ molecule calculated at B3LYP/ 6–311++G (d,p) level of theory.

Fig. 3. d_{norm} cartography (a) and d_e cartography (b) of BD(NO_3)$_2$.

Fig. 4. Percentage of all contacts and atoms present in the BD(NO_3)$_2$ material.

Fig. 5. Reduced density gradient and isosurface density plot along with the color filled scale bar defining interaction limits for the BD(NO_3)$_2$ compound.

Fig. 6. Cole-Cole plots (a), plots of the real and imaginary parts of impedance Z’ (b) and Z’’ (c) vs log(f), of BD(NO_3)$_2$ at various temperatures.

Fig. 7. Variation of the real part M’(a) and imaginary parts M’’(b) of the electric modulus and variation of dielectric complex permittivity ε’(a) and ε’’(b) as a function of the frequency at various temperatures in $BD(NO_3)_2$.

Fig. 8. IR spectra of $BD(NO_3)_2$ molecule.

Fig. 9. The best docked pose of $BD(NO_3)_2$ with different Fungal.

Fig. 10. Different types of interactions between $BD(NO_3)_2$ and different Fungal.

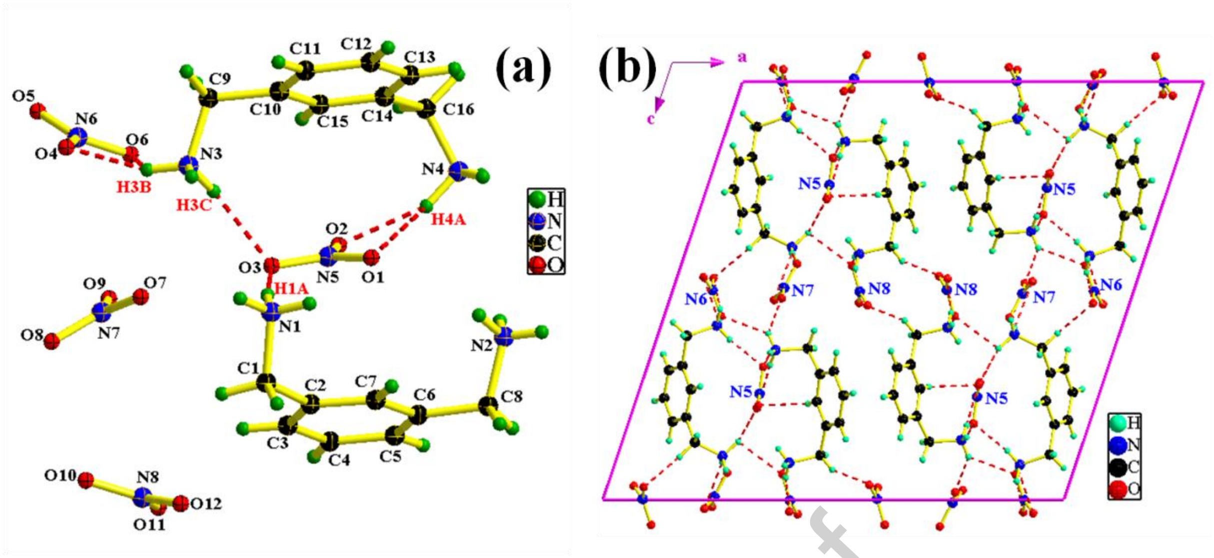
(a)
O5
N6
O6
O4
H3B
C9
N3
H3C
C11
C12
C13
C10
C15
C14
C16
N4
H4A
O2
O3
N5
O1
H1A
O9
O7
O8
N7
N1
N2
C1
C2
C7
C6
C8
C3
C4
C5
O10
N8
O12
O11
H
N
C
O
(b)
a
c
N5
N6
N7
N8
N8
N7
N6
N5
N5
N5
H
N
C
O

Fig. 1

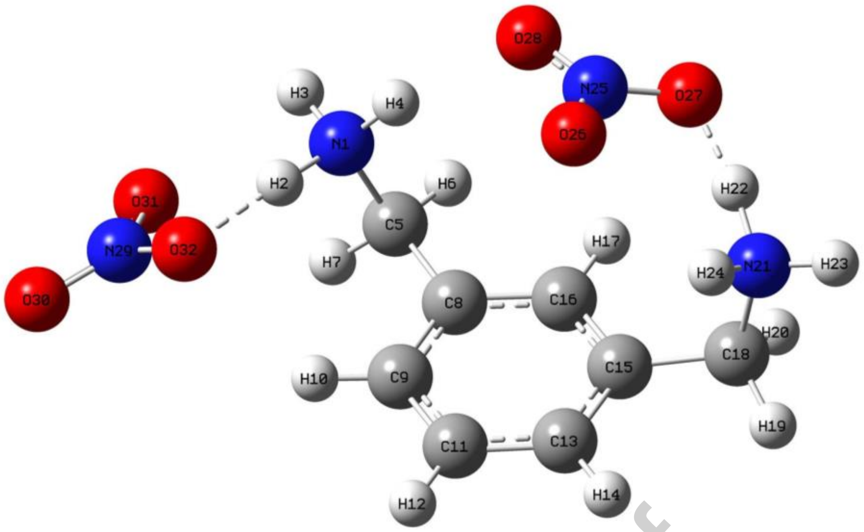
O28
N25
O27
O26
H3
H4
N1
H2
H6
O31
C5
H17
H22
N29
O32
H7
H24
N21
H23
O30
C8
C16
H20
C15
C18
H10
C9
C11
C13
H19
H12
H14

Fig. 2

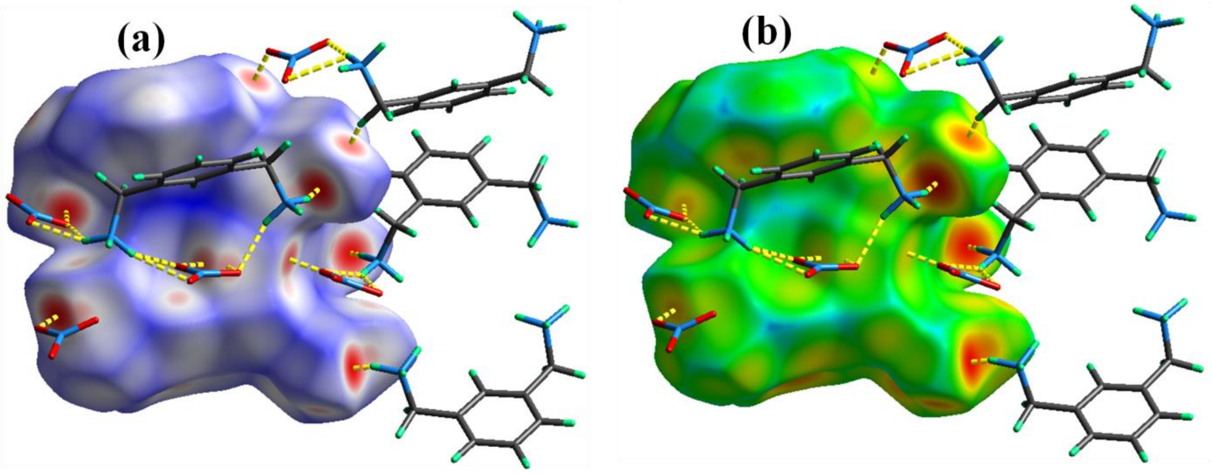

Fig. 3

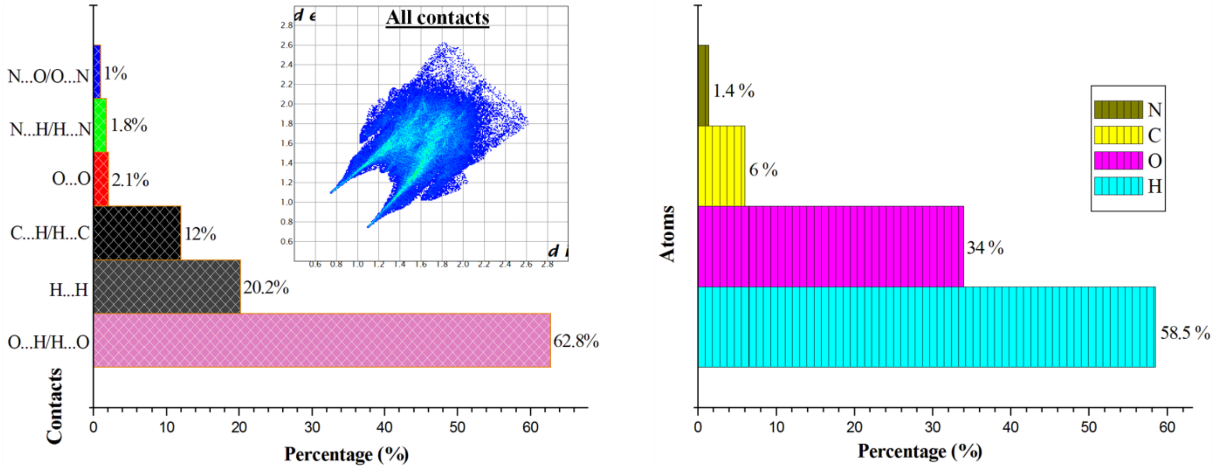
All contacts
d e
d i
N...O/O...N 1%
N...H/H...N 1.8%
O...O 2.1%
C...H/H...C 12%
H...H 20.2%
O...H/H...O 62.8%
Contacts
Percentage (%)
0
10
20
30
40
50
60
Atoms
1.4 %
6 %
34 %
58.5 %
N
C
O
H
Percentage (%)

Fig. 4

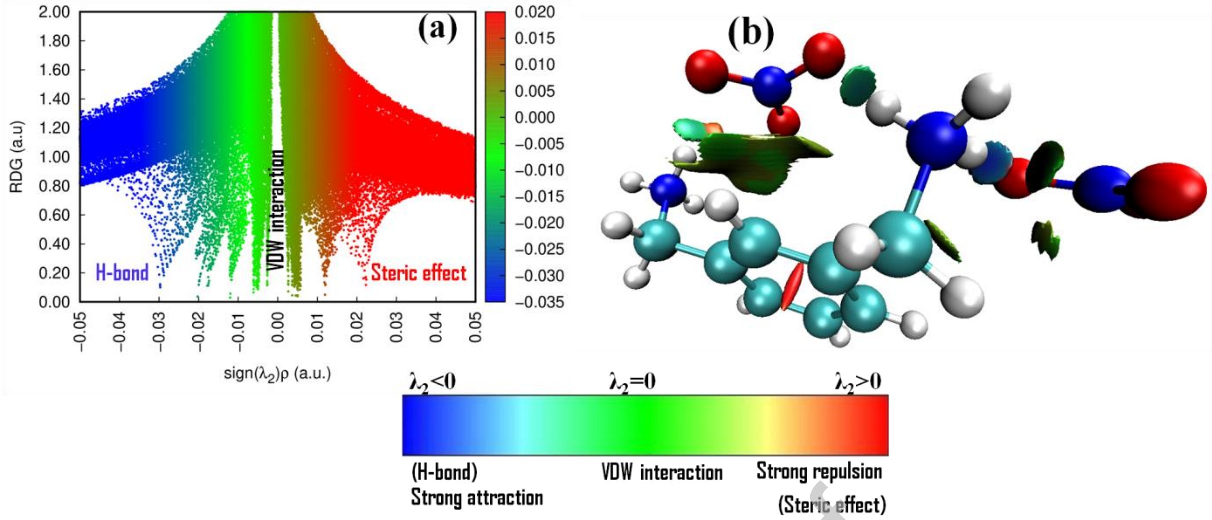
(a)
2.00
1.80
1.60
1.40
1.20
1.00
0.80
0.60
0.40
0.20
0.00
RDG (a.u)
−0.05
−0.04
−0.03
−0.02
−0.01
0.00
0.01
0.02
0.03
0.04
0.05
sign(λ2)ρ (a.u.)
H-bond
VDW interaction
Steric effect
0.020
0.015
0.010
0.005
0.000
−0.005
−0.010
−0.015
−0.020
−0.025
−0.030
−0.035
(b)
λ2<0
λ2=0
λ2>0
(H-bond)
Strong attraction
VDW interaction
Strong repulsion
(Steric effect)

Fig. 5

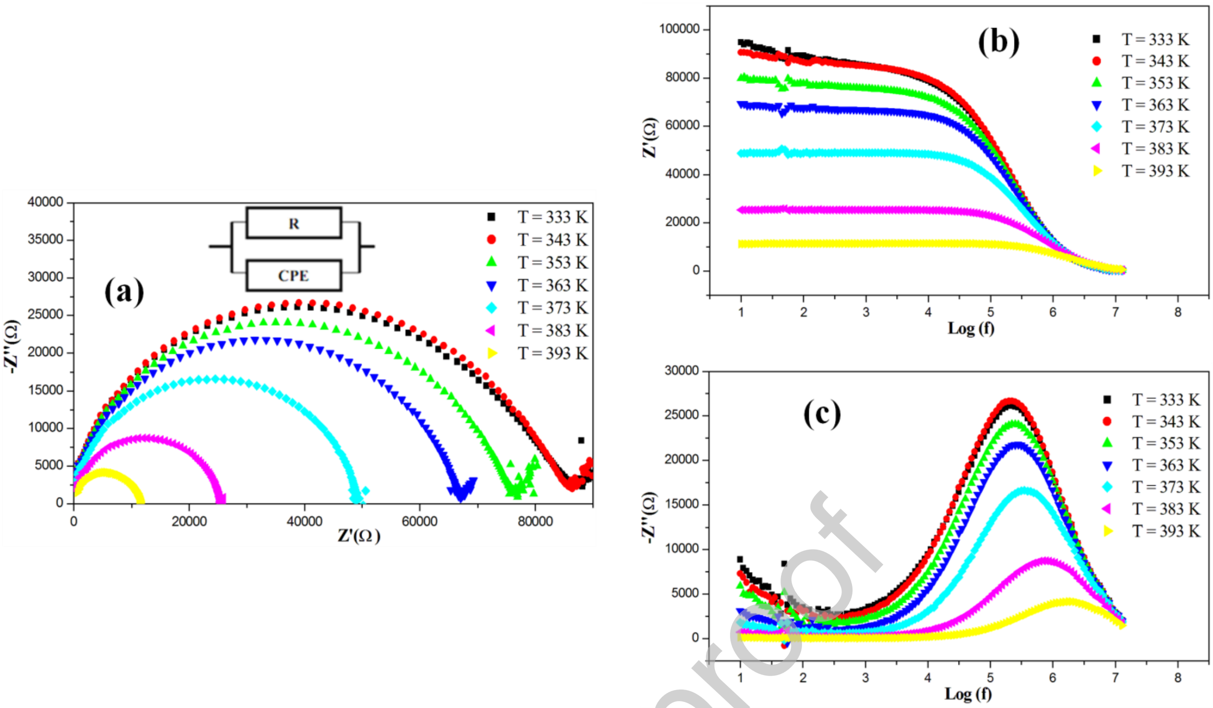
(a)
R
CPE
-Z''(Ω)
Z'(Ω)
0
5000
10000
15000
20000
25000
30000
35000
40000
0
20000
40000
60000
80000
T = 333 K
T = 343 K
T = 353 K
T = 363 K
T = 373 K
T = 383 K
T = 393 K
(b)
Z'(Ω)
Log (f)
0
20000
40000
60000
80000
100000
1
2
3
4
5
6
7
8
(c)
-Z''(Ω)
Log (f)
0
5000
10000
15000
20000
25000
30000

Fig. 6

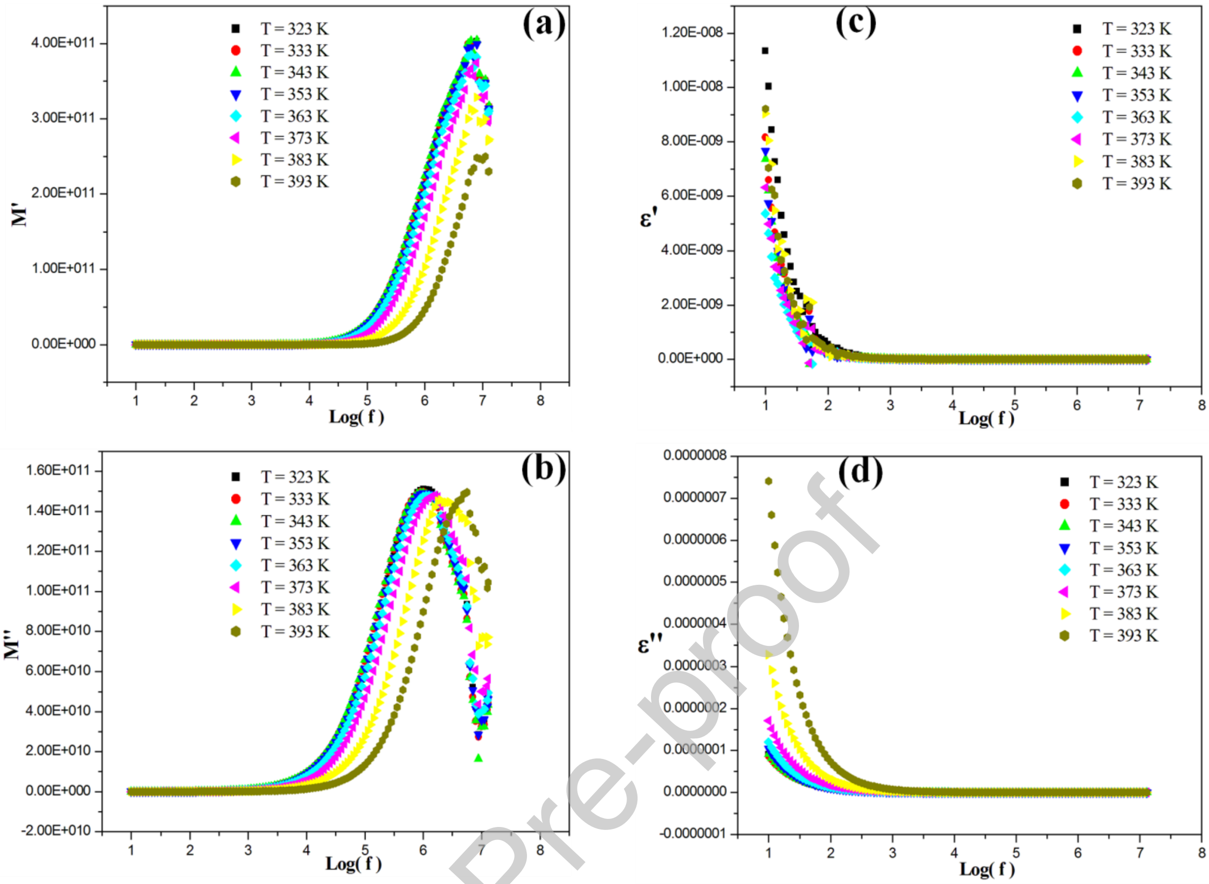
(a)
M'
4.00E+011
3.00E+011
2.00E+011
1.00E+011
0.00E+000
Log(f)
T = 323 K
T = 333 K
T = 343 K
T = 353 K
T = 363 K
T = 373 K
T = 383 K
T = 393 K
(b)
M''
1.60E+011
1.40E+011
1.20E+011
1.00E+011
8.00E+010
6.00E+010
4.00E+010
2.00E+010
0.00E+000
-2.00E+010
Log(f)
(c)
ε'
1.20E-008
1.00E-008
8.00E-009
6.00E-009
4.00E-009
2.00E-009
0.00E+000
Log(f)
(d)
ε''
0.0000008
0.0000007
0.0000006
0.0000005
0.0000004
0.0000003
0.0000002
0.0000001
0.0000000
-0.0000001
Log(f)
1
2
3
4
5
6
7
8

Fig. 7

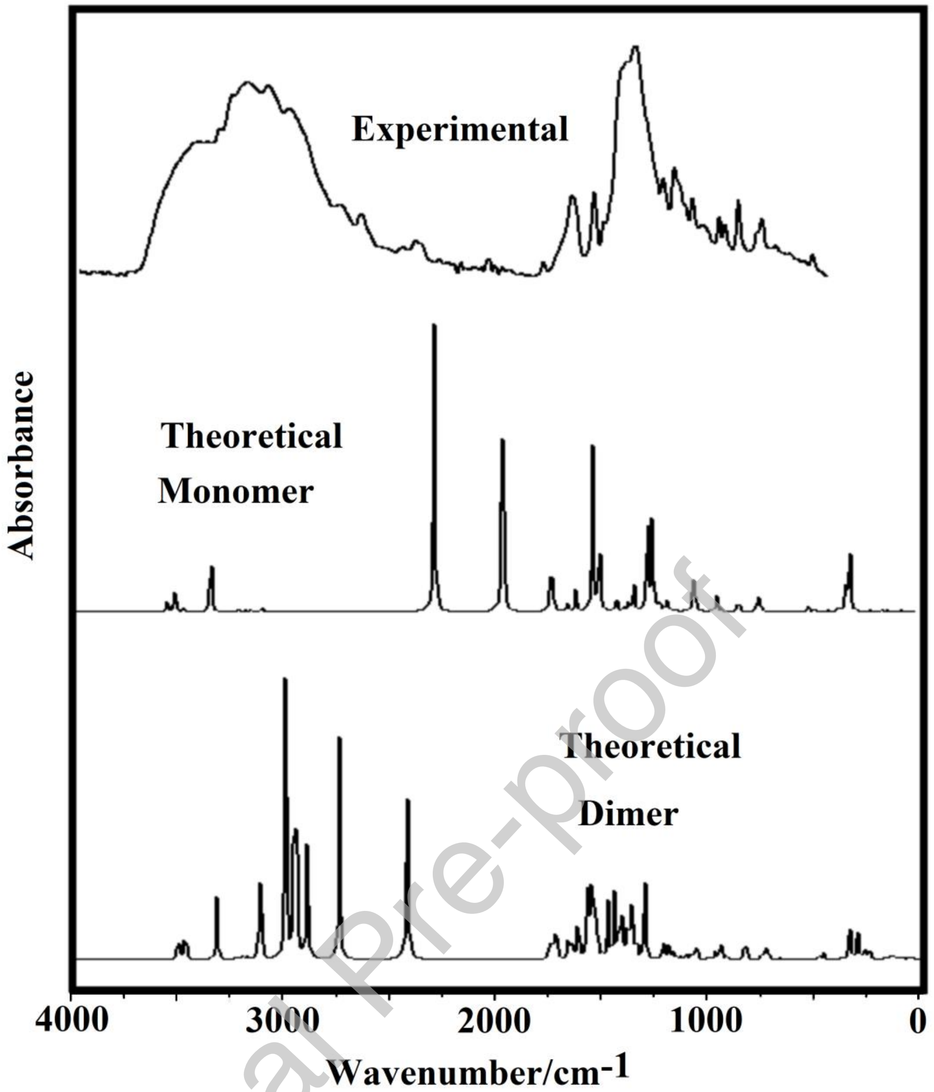
Experimental
Theoretical
Monomer
Theoretical
Dimer
Absorbance
4000
3000
2000
1000
0
Wavenumber/cm-1

Fig. 8

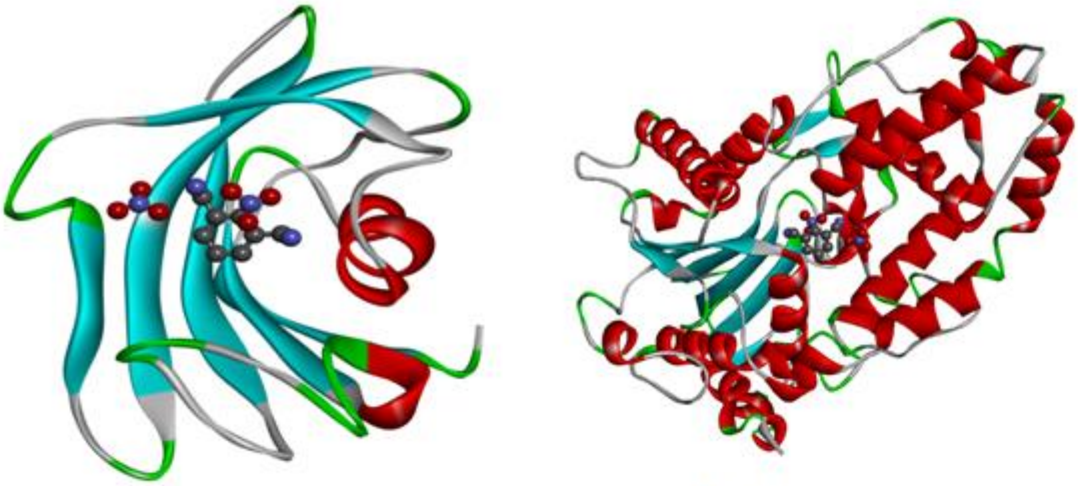

(a) 5HWC (b) 3K4Q

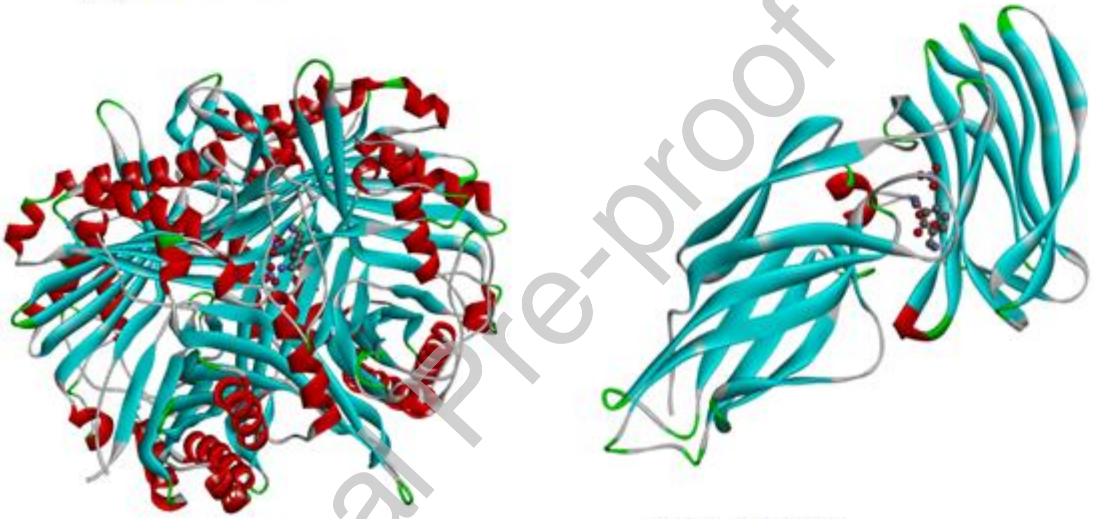

(c) 1XY3 (d) 4LEB

Fig. 9

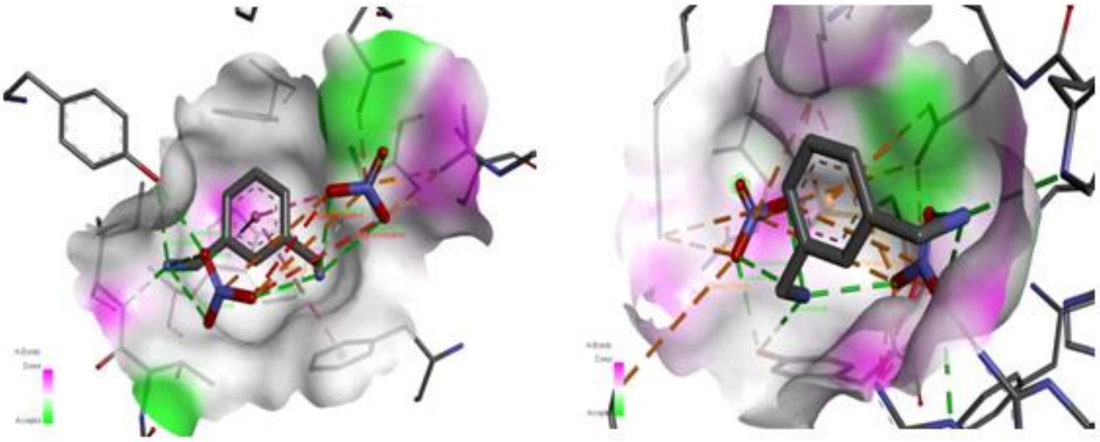

(a) 5HWC

(b) 3K4Q

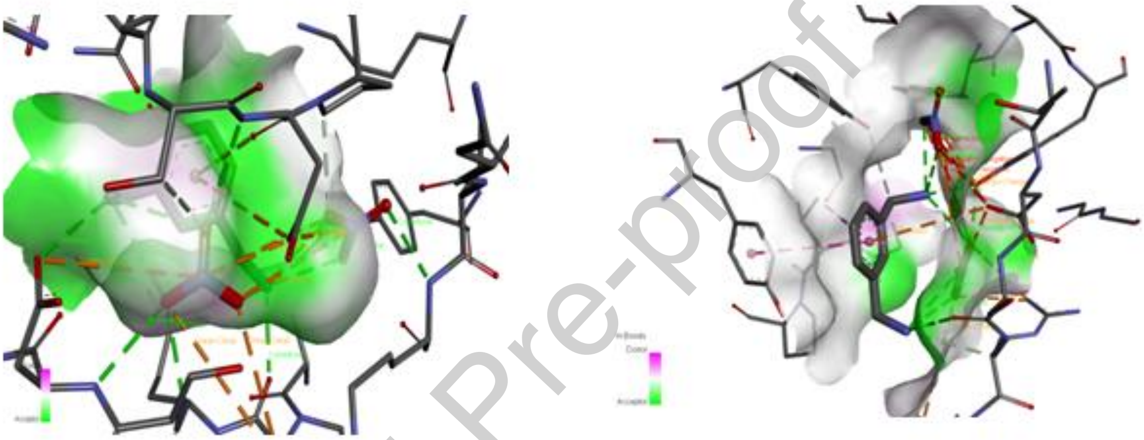

(c) 1XY3

(d) 4LEB

Fig. 10

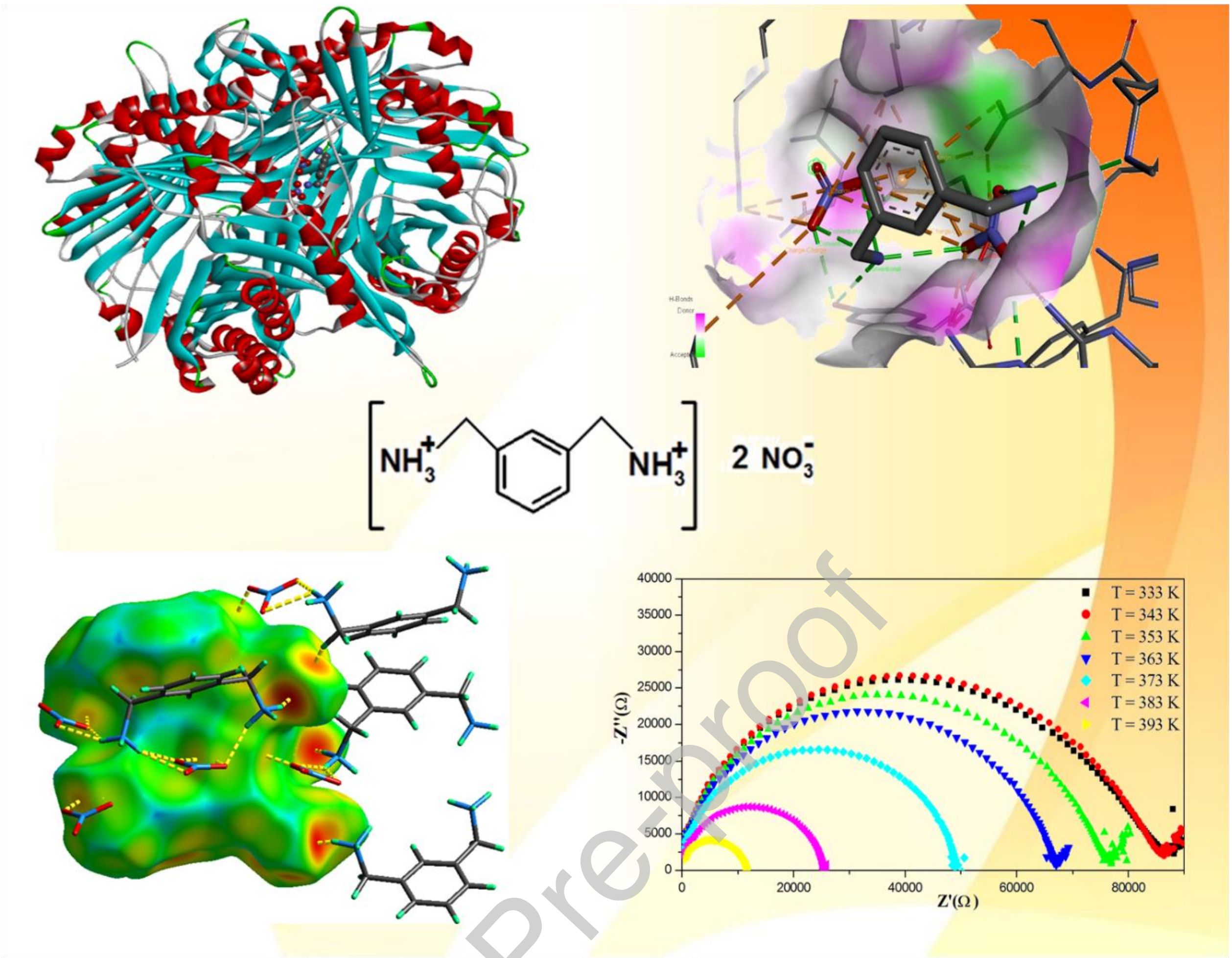

Graphical abstract